Coseismic and postseismic slip as a likely trigger of a 1 slow slip event (M 5.5) on the Longitudinal Valley

Alexandre Canitano[1], Maxime Godano[2], and Marion Y Thomas[3]

[1]Institute of Earth Sciences, Academia Sinica
[2]Université Côte d'Azur
[3]Sorbonne Université, CNRS-INSU

November 24, 2022

Abstract

Using borehole strainmeters, we detected a 13-day long slow slip event on the Longitudinal Valley Fault, Taiwan. It is located between 8 to 15 km depth and has an equivalent moment magnitude of 5.5. The slow event has likely been promoted by the significant Coulomb stress changes (+ 1 MPa) imparted by a combination of coseismic and postseismic slip of the M w 6.8 Chengkung earthquake. Besides, insignificant coseismic slip is observed in the slow event region, suggesting that the latter could have acted as a barrier during the Chengkung earthquake. We also found a spatiotemporal correlation between the slow event and a cluster of repeating microearthquakes, suggesting aseismic slip as a possible driven mechanism of repeating ruptures. These results highlight the complex interplay between seismic and aseismic processes along the fault.

Coseismic and postseismic slip as a likely trigger of a slow slip event (M 5.5) on the Longitudinal Valley Fault, Taiwan

Alexandre Canitano[1], Maxime Godano[2] and Marion Y. Thomas[3]

Corresponding author: A. Canitano, Institute of Earth Sciences, Academia Sinica, Nankang, Taipei, Taiwan. (canitano@earth.sinica.edu.tw)

[1]Institute of Earth Sciences, Academia Sinica, Nankang, Taipei, Taiwan.

[2]Université Côte d'Azur, CNRS, Observatoire de la Côte d'Azur, IRD, Géoazur, 250 rue Albert Einstein, Sophia Antipolis 06560 Valbonne, France.

[3]Sorbonne Université, CNRS-INSU, Institut des Sciences de la Terre Paris, ISTeP UMR 7193, F-75005 Paris, France.

Using borehole strainmeters, we detected a 13-day long slow slip event on the Longitudinal Valley Fault, Taiwan. It is located between 8 to 15 km depth and has an equivalent moment magnitude of 5.5. The slow event has likely been promoted by the significant Coulomb stress changes ($\sim +1$ MPa) imparted by a combination of coseismic and postseismic slip of the M_w 6.8 Chengkung earthquake. Besides, insignificant coseismic slip is observed in the slow event region, suggesting that the latter could have acted as a barrier during the Chengkung earthquake. We also found a spatiotemporal correlation between the slow event and a cluster of repeating microearthquakes, suggesting aseismic slip as a possible driven mechanism of repeating ruptures. These results highlight the complex interplay between seismic and aseismic processes along the fault.

1. Introduction

Over the last two decades, the growing development of dense geodetic and seismological monitoring arrays in active regions has revealed episodic aseismic slip in the crust, spanning timescales from seconds to years [e.g., *Peng and Gomberg*, 2010]. These slow slip events (SSEs), which play an important role in redistributing stress in the Earth's crust [e.g., *Linde et al.*, 1996], are now observed in various tectonic regions and fault environments [e.g., *Bürgmann*, 2018]. SSEs are often accompanied by earthquake swarms [*Vallée et al.*, 2013; *Gualandi et al.*, 2017; *Fasola et al.*, 2019] or nonvolcanic tremors [e.g., *Beroza and Ide*, 2011], and together, represent an important mechanism of strain release in active regions. Therefore, investigating the stress conditions, the faulting mechanisms of slow slip and what role they play in the earthquake cycle is fundamental to determine time-dependent earthquake hazard.

In eastern Taiwan, the Longitudinal Valley (LV) is an active collision boundary between the Eurasian and Philippine Sea plates [*Barrier and Angelier*, 1986], and accounts for more than half of the 9 cm.yr^{-1} of oblique plate convergence [*Yu et al.*, 1997]. The Longitudinal Valley Fault (LVF), which runs along the eastern side of the LV, represents the major active structure in the region and accounts for about 4.5 cm.yr^{-1} of total plate convergence [*Thomas et al.*, 2014] (Figure 1). The fault is creeping at the surface at the rate of 1-6 cm/yr between latitudes 23°00′ and 23°30′ [*Thomas et al.*, 2014] and also experiences seasonal and transient creep episodes [*Lee et al.*, 2003; *Murase et al.*, 2013]. Despite significant historical earthquakes, there is a paucity of large shocks along the fault relatively to the high convergence rate, suggesting that a significant fraction of the long-term slip rate, in the seismogenic depth range, is released aseismically [*Liu et al.*, 2009]. Indeed, based on the analysis of geodetic data for the 1992-2010 period, *Thomas et al.* [2014] demonstrate that a major fraction of the long-term slip budget (80-90%) on the southern section of the LVF is the result of aseismic slip. Following the 2003 M_w 6.8 Chengkung earthquake, a 7-year long afterslip has been detected by Global Positioning System (GPS) stations along the Chihshang Fault (CF) [*Thomas et al.*, 2014], a 30-km long section of the southern LVF. Borehole strainmeters have captured a very shallow SSE (2 to 4 km depth) with geodetic moment magnitude $M \sim 4.5$ in central LV [*Canitano et al.*, 2019]. A 1-month long afterslip following a M_w 4.6 earthquake on the CF was also shown to control the rate of aftershocks near the earthquake source region [*Canitano et al.*, 2018a]. However, the dearth of aseismic transient observations in the region strongly limits our ability to investigate the mechanisms of deformation along the fault and to further interpret the interplay between seismic and aseismic processes.

In this study, we document a 2-week long SSE with an equivalent moment magnitude of 5.5. It occurred in January-February 2011 on the central section of the LVF, northeast of the source rupture of the 2003 Chengkung earthquake. This event occurred between 8 to 15 km depth and was detected by borehole strainmeters deployed in two networks distant by about 35 km. Using static Coulomb stress modeling, we investigate a possible contribution of coseismic and postseismic slip of the Chengkung event to the SSE occurrence. We also analyze the spatiotemporal pattern of a cluster of earthquake multiplets occurring during the SSE episode and investigate its relationship with aseismic slip.

2. Near-fault instrumentation and data processing

Beginning in 2003, to shed additional light on the nature of the deformation in the LV, the Institute of Earth Sciences (IES) Academia Sinica, in cooperation with the Department of Terrestrial Magnetism, Carnegie Institution of Washington, has deployed 11 *Sacks-Evertson* [*Sacks et al.*, 1971] borehole strainmeters along the LVF (Figure 1). They monitor rock volume change (dilatation ϵ_v) and complement the GPS measurements for detecting crustal transients at short to intermediate periods (minutes to weeks). Identifying SSEs requires a careful separation of noise and various environmental signals in the geodetic time-series. We calibrate the dilatometers using solid-Earth and ocean tides [*Canitano et al.*, 2018b] (Figure S1), and process the strain data to correct for borehole relaxation, to remove solid-Earth and ocean tidal strain and air pressure induced strain. Hydrological variations induce strain changes larger than hundreds of nanostrain (nϵ) [*Hsu et al.*, 2015], that should be quantified and corrected when necessary. Groundwater level changes are recorded by hydrological stations deployed by the Water Resources Bureau in Taiwan. Rainfall stations are operated by the Central Weather Bureau (CWB) in Taiwan, and sea level changes are continuously monitored by a tide gauge installed near Chengkung and operated by the CWB. The corrected strain signals and environmental signals are presented in Figure 2. We process the GPS data with the GAMIT10.42/GLOBK5.16 software packages [*Herring et al.*, 2010] using the 2005 International Terrestrial Reference

Frame (ITRF2005) [*Altamini et al.*, 2007] coordinates in GLOBK processing (Figure S2).

3. Detection and characterization of the SSE

Starting on 29 January 2011, we observe a dilatation of 49 nϵ at the SSTB station while ZANB strainmeter recorded a contraction of -39 nϵ (Figure 2a). A moderate strain contraction ($\sim$ -10 nϵ) is also visible on HGSB signal while FBRB did not record any relevant signal (SSNB and CHMB experienced a power outage). The sudden and gradual volumetric changes occurred during a period of minimum precipitation as expected during the dry season (October to April). Only a very light rainfall ($<$ 1 mm/hr) occurred during days 28.1 to 28.9 in the valley (Figure 2b), and induced a low contraction at SSTB and ZANB ($\sim$ -5 nϵ and -10 nϵ, respectively). However, the mass loading of rainwater induces contractional strain in the crust [*Mouyen et al.*, 2017], while SSTB recorded dilatational strain. Therefore, the observed strain changes are not associated with precipitation and, neither are they induced by hydrology as no transient change in groundwater level is detected during January-February 2011 (Figure 2b). There are also no appreciable sea level changes during the SSE episode. The largest variations occurred during days 34 to 35 ($\sim$ 0.1 m) and remain undetected by near-coastal stations (ZANB and SSTB) (Figure 2c).

Sudden changes in strain excursions are visible around day 29.06 and have nearly similar temporal evolution until day $\sim$ 41.8 (Figure 2d), which corresponds to the timing for which signals recorded by ZANB and HGSB simultaneously stopped their evolution (SSTB experienced a power outage during days 42-47). We are however not able to resolve the SSE onset with a precision better than a few hours since the SSE may have started during the light rain episode (Figure S3). Nonetheless, rainfall-induced strain during day 28 is low and has likely no influence on the final amplitude of the SSE signals. Therefore, coherent strain changes over 13 days, unrelated to environmental changes, are observed in two networks distant by about 35 km, and therefore likely represent the signature of a slow transient deformation. The SSE has not been detected by the GPS stations in the region (Figure S2).

We estimate the optimal source location and magnitude (i.e., source dimensions and aseismic slip) using a grid search approach. We search for a source compatible with the LVF with a strike of 23°NE and a geologic rake of 70°, which corresponds to the mean slip vector direction in the Yuli-Fuli region [*Peyret et al.*, 2011]. At each step, we calculate the dilatation at the sensor locations resulting from a static dislocation in an elastic homogeneous half-space for a planar rectangular fault with uniform slip [*Okada*, 1992], and estimate the absolute difference between observed and predicted strain (residual strain) to infer the best source model (Section S1). Our preferred source (with residual strain < 1.2 nϵ and maximal surface displacements ≤ 1.9 mm for CHGO) is located between 8 and 15 km depth, it has length (L) and width (W) of 12 km x 8 km, respectively, and a total displacement of $D = 7.5$ cm. The depth of the source is particularly well constrained, even with a limited number of stations, as buried sources result in dilatation that changes sign at distances strongly dependent on the source depth. Insignificant change recorded by FBRB is thus explained by a nodal plane passing through the station location (Figure S5). The SSE has a geodetic moment magnitude of 5.5, a typical value for a 2-week long SSE [*Bürgmann*, 2018; *Michel et al.*, 2019] and verifies an earthquake-like cubic moment-duration scaling, as reported in Cascadia [*Michel et al.*, 2019; *Dal Zilio et al.*, 2020] and Mexico [*Frank and Brodsky*, 2019]. We compute the static stress drop $\Delta\sigma$ following *Madariaga* [1977]:

$$\Delta\sigma = \frac{8}{3\pi} G \frac{D}{W} \tag{1}$$

The average stress drop ranges from 0.19 MPa to 0.37 MPa with $\Delta\sigma = 0.23$ MPa for our best source model. This is consistent with values predicted by *Gao et al.* [2012] for aseismic moment versus fault area scaling laws.

We search for recurrent events using a geodetic template matching but found no additional events (Section S2). At the minimum, the recurrence time of such event is about 7 to 8 years. Our search is however limited by the strain templates allowing only to detect events with nearly similar duration and location as the 2011 SSE. We cannot exclude neither that our method failed to detect recurrent events with lower magnitude. Indeed, such signals are below the GPS ambient noise level and frequent rainfall strongly impact strainmeter records, potentially concealing transient signals.

4. Influence of static stress changes from the 2003 Chengkung earthquake

The SSE occurred at a distance of about 10 km from the epicenter of the December 2003 M_w 6.8 Chengkung earthquake. The mainshock was followed by an afterslip with an aseismic moment equivalent to 0.8 times the seismic moment at the end of the study period (end of November 2010) [*Thomas et al.*, 2014, 2017]. The SSE occurred two months after the end of the study period while some parts of the fault were still creeping at higher rate than during the preseismic period [*Thomas et al.*, 2014, 2017]. Given that SSEs are highly sensitive to small stress perturbations (a few kPa) [e.g., *Hawthorne and Rubin*, 2010], we estimate the contribution of coseismic and postseismic slip to the SSE occurrence using the Coulomb failure criterion. If $\delta\sigma_n$ and $\delta\tau$ represent respectively the changes in normal stress (tensile stress is positive) and shear stress on the fault plane (positive in the direction of the long-term fault slip) induced by the cumulative slip, then according to the Coulomb failure criterion, the static Coulomb stress change δCFF is defined as:

$$\delta CFF = \delta\tau + \mu^{'}\delta\sigma_n \tag{2}$$

where $\mu^{'}$ is the effective friction coefficient, here taken as 0.4. The fault moves closer to failure if $\delta CFF > 0$ and away from failure if $\delta CFF < 0$. δCFF is resolved onto the LVF plane using *Coulomb 3.3* [*Toda et al.*, 2005; *Lin and Stein*, 2004] for a rake angle parallel to the geologic slip vector of the SSE, using the coseismic and postseismic slip distribution models from *Thomas et al.* [2014].

The time-evolution of postseismic slip is modeled using 7 years of geodetic data following the mainshock. Thus, modeled δCFF represents a very close estimate of the static stress changes on the fault at the SSE onset timing (only 2 out of 86 months of afterslip are missing). Moreover, it is worth noticing that this model predicts the cumulative stress as if it had occurred instantaneously and does not account for the complex interactions between fault plane patches that occurred over the 7 years of afterslip. The SSE source is located in an area of very low coseismic slip (≤ 0.1 m) and moderate cumulative postseismic slip (about 0.2-0.4 m during the 7-yr period) (Figure 3). The source also lies in an area where coseismic and postseismic slip induced a positive δCFF exceeding of 0.3 MPa and 0.5 MPa, respectively.

5. Analyze of earthquake multiplets during the SSE episode

We analyze the seismicity during the SSE episode and find no evidence for the occurrence of nonvolcanic tremors or for a temporary increase in seismicity (Figure S7). Additionally, we search for possible repeating earthquakes (REs), which consist of repeated ruptures of the same asperity, and represent velocity-weakening regions that rupture repeatedly, embedded in an otherwise velocity-strenghtening region [e.g., *Beeler et al.*, 2001]. REs illuminate the spatiotemporal behaviour of aseismic slip [*Uchida and Bürgmann*, 2019]. We calculate the cross-correlation coefficients (*ccc*) of the vertical velocity signals for all earthquake pairs for stations FULB, YULB, CHKH and ELDB. We filter the 100-Hz sampling signals between 3 and 20 Hz to suppress microseismic noise and the cross-correlation window has a length of 2 s and begins 0.1 s before manual P-wave picks. Three events (over 12) show high waveform coherence ($ccc \sim$ 0.88-0.98) at all the stations (Figure 4a). They occurred during a 40-min period on 5 February 2011 (day 36) and have local magnitude $M_L < 2$ (events 1-3, Table S1).

To further characterize the earthquake multiplet, we search for additional events for the 2003-2019 period using waveform template matching. We use event 1 as template and perform sliding-window cross correlations [*Yang et al.*, 2009] for 10 broadband seismic stations (Figure 1). New events are added to the multiplet if their P-wave cross correlation coefficient is higher than 0.75, at minimum, for two stations. We find a total of 32 events (Table S1 and Figure S8). The multiplet is relocated using the double-difference algorithm *HypoDD* [*Waldhauser and Ellsworth*, 2000] with manually picked P- and S-wave absolute arrival times and relative P- and S-wave delay times. The relative times are determined by cross-correlating all earthquakes pairs in the multiplet ($ccc > 0.75$ for at least 2 stations). It corresponds to 403 pairs, among which 50% (202 pairs) show high similarity for 3 stations or more. To ensure a good constraint on the absolute location of the multiplet, we jointly relocate it with 100 earthquakes selected near and within the SSE source (Figure S9). For these additional earthquakes, only manually picked P- and S- arrival times are inverted.

As a result, 22 events of the multiplet are relocated at the depth of about 14.5 km inside a $\sim$ 300 m x 200 m area roughly dipping 50° southeastward (Figure 4b), which is compatible with the geometry of the LVF. We assess the relative location uncertainties by a bootstrap resampling method following *Waldhauser and Ellsworth* [2000] for two types of uncertainties (see Figure S10 for details). First is the relative uncertainty inside the multiplet, assessed by bootstrapping residual times from the relocation of the multiplet without the additional earthquakes. Second is absolute uncertainty of the multiplet location estimated from the bootstrapping performed on the joint relocation. We obtain relative horizontal and vertical uncertainties of about 20 m and 27 m, and absolute horizontal and vertical uncertainties of about 150 m and 200 m, respectively.

6. Discussion and concluding remarks

The 2003 Chengkung earthquake represents the largest event impacting the LVF during the past decades. It generated maximum static Coulomb stress perturbations in the SSE source region two orders of magnitude larger than any other regional $M_w > 6$ earthquake or aseismic event (Figure S11). We propose that the SSE occurrence has been promoted by the significant Coulomb stress changes ($\delta CFF \sim +1$ MPa, about 4 times greater than the SSE average stress drop) imparted by a combination of coseismic and postseismic slip from the earthquake, and which persists several years after the mainshock. Further, since afterslip dominates the Chengkung postseismic relaxation [*Thomas et al.*, 2014], the slow loading process is largely dominated by the large elastic stress redistribution following the mainshock rather than by viscoelastic stress transfer [e.g., *Freed and Lin*, 2001].

Coseismic static stress changes are permanent perturbations, with effects lasting from days to years [e.g., *Segou and Parsons*, 2020], and can therefore explain an extended period for triggering of aftershocks [*King et al.*, 1994] and SSEs [*Hayes et al.*, 2014; *Rolandone et al.*, 2018]. Besides, long-lasting stress effects from postseismic deformation can also play a significant role in promoting delayed rupture [*Segou and Parsons*, 2018]. The 2017 M_w 7.1 Puebla earthquake, Mexico, was likely triggered by postseismic stress changes (up to 0.1 MPa) following the 2012 M_w 7.5 Oaxaca event [*Segou and Parsons*, 2018], while a combination of postseismic stress changes from the 1964 M_w 9.2 Alaska earthquake and a 12 year-long SSE possibly promoted the 2018 M_w 7.1 Anchorage earthquake [*Segou and Parsons*, 2020]. Finally, since no strain data are available shortly following the mainshock, we cannot rule out the possibility that SSEs have also already occurred in the early stage of the seismic cycle [*Voss et al.*, 2017], while stress conditions in the SSE region were already favourable for promoting rupture.

The multiplet is located in an area of negative Coulomb stress changes imparted by the SSE (Figure S12). Because the horizontal separation between the multiplet location and the positive Coulomb stress lobe ($\sim$ 1 km) is much larger than the resolution of the SSE plane horizontal location (about 200 m), we can rule out a possible triggering through Coulomb stress transfer. On the other hand, given the largest uncertainties on the vertical locations of the cluster and the SSE source, sources can be spatially co-located. This would suggest that the 40-min burst of earthquakes is likely the result of recurrent seismic ruptures to accommodate aseismic slip in the surrounding area [e.g., *Beeler et al.*, 2001]. Postseismic slip was proposed as a likely driven mechanism of repeating earthquakes in the region following small-magnitude earthquakes [*Canitano et al.*, 2018a]. However, similar earthquake sequences are also observed in 2005, 2008, 2014 and 2016 in the absence of aseismic slip (Figure S6). This periodicity of 2-3 years coincides with observations for repeater sequences unrelated to geodetic transients [*Chen et al.*, 2009, 2020]. Therefore, we cannot exclude that ruptures occurred spontaneously, earthquakes rupturing close-by, but distinct, asperities in a triggering cascade of ruptures [e.g., *Lengliné and Marsan*, 2009].

In addition to triggering aseismic slip, the Chengkung earthquake had also impacted the dynamics of repeater sequences along the LVF, notably halving their recurrence interval [*Chen et al.*, 2020]. However, the absence of additional transient signals and the resolution limits for microseismicity analysis impact our ability to further interpret the complex interplay between seismic and aseismic processes on the fault, and their relationship with the Chengkung rupture (Figure 4c).

The source region of the SSE coincides with a region of low interseismic coupling (< 0.2) while the Chengkung rupture area coincides with high coupling (Figure S13a). We can note that in 2011, the fault region hosting the SSE has accumulated about 0.3 m of slip deficit (Figure S13b), mainly due to the 7-yr postseismic slip. A limited fraction (about 20%) of this deficit has been accommodated by the SSE, and additional and/or recurrent SSEs as well as postseismic slip should likely help to release the remaining slip deficit. Further, the SSE region lies in an area of moderate afterslip, suggesting that areas of the fault zone experiencing afterslip can also host SSEs [*Yarai and Ozawa*, 2013; *Rolandone et al.*, 2018]. Conversely, insignificant coseismic slip is observed in the SSE region. Thus, the region could have acted as a barrier, impeding the Chengkung rupture to propagate further northeast, as observed during some megathrust earthquakes [*Dixon et al.*, 2014; *Rolandone et al.*, 2018; *Perfettini et al.*, 2010]. However, further analysis are needed to decipher whether a dominant aseismic slip mode prevails throughout the earthquake cycle for the transient slow slip zone [e.g., *Rolandone et al.*, 2018] (i.e., a permanent barrier), or if seismic ruptures can partially or completely penetrate it [e.g., *Lin et al.*, 2020].

To conclude, we document the largest SSE detected onshore Taiwan to date. A SSE was detected at the transition between the aseismic, creeping section of the LVF and the locked zone [*Canitano et al.*, 2019], we now show evidence that the fault can also host larger events at seismogenic depths. Better monitoring and characterizing slow transient events is fundamental to identify areas with high seismic hazard on the LVF, to connect SSEs to large, destructive earthquakes [e.g., *Radiguet et al.*, 2016], and to understand how they contribute to relieve the long-term strain budget of the fault.

Acknowledgments

We thank Alan Linde, Selwyn Sacks and the support staff of the Carnegie Institution of Washington for the construction, installation, and maintenance of the dilatometers, and Hsin-Ming Lee for collecting the strainmeter data. The authors acknowledge Yi-Chuen Tsai and Mei-Jun Yu for processing the GPS data and Ya-Ju Hsu for providing codes for visualizing seismicity. We are grateful to Kate Chen and Yaochieh Chen for providing the repeater catalog. We thank Wen-Tzong Liang and Wen-Hui Lee for the access to the seismological data. Some figures were drawn using the Generic Mapping Tools [*Wessel and Smith*, 1998]. Strainmeter data are available at *dmc.earth.sinica.edu.tw* and broadband seismological data are available at *http://tecws1.earth.sinica.edu.tw/IESWS* (BATS network [*Institute of Earth Sciences, Academia Sinica, Taiwan*, 1996]). This research is supported by the Ministry of Science and Technology grant MOST 108-2116-M-001-027-MY2. This is the contribution of the Institute of Earth Sciences, Academia Sinica, IESASXXXX.

References

Altamini, Z., X. Collilieux, J. Legrand, B. Garayt and C. Boucher (2007), ITRF2005: A new release of the International Terrestrial Reference Frame based on time series of station positions and Earth Orientation Parameters, *J. Geophys. Res.*, *112*, B09401, doi:10.1029/2007JB004949.

Barrier, E. and J. Angelier (1986), Active collision in eastern Taiwan: the Coastal Range, *Tectonophysics*, *125*, 39–72.

Beroza, G. C. and S. Ide (2011), Slow earthquakes and nonvolcanic tremors, *Annu. Rev. Earth Planet. Sci.*, *39*, 271–296.

Beeler, N. M., D. A. Lockner and S. H. Hickman (2001), A simple stick-slip and creep slip model for repeating earthquakes and its implication for micro-earthquakes at Parkfield, *Bull. Seism. Soc. Am.*, *91*, 1797–1804.

Bürgmann, R. (2018), The geophysics, geology and mechanics of slow fault slip, *Earth Planet. Sci. Lett.*, *495*, 112–134.

Canitano, A., M. Godano, Y. J. Hsu, H. M. Lee, A. T. Linde and S. Sacks (2018a), Seismicity controlled by a frictional afterslip during a small magnitude seismic sequence ($M_L < 5$) on the Chihshang Fault, Taiwan, *J. Geophys. Res. Solid Earth*, *123*(2), 2003–2018, doi:10.1002/2017JB015128.

Canitano, A., Y. J. Hsu, H. M. Lee, A. T Linde and S. Sacks (2018b), Calibration for the shear strain of 3-component borehole strainmeters in eastern Taiwan through Earth and ocean tidal waveform modeling, *J. Geodesy*, *92*(3), 223–240.

Canitano, A., H. Gonzalez-Huizar, Y. J. Hsu, H. M. Lee, A. T. Linde and S. Sacks (2019), Testing the influence of static and dynamic stress perturbations on the occurrence of a shallow, slow slip event in eastern Taiwan, *J. Geophys. Res. Solid Earth*, *124*(3), 3073–3087, doi:10.1029/2018JB016742.

Chen, K. H., R. J. Rau and J. C. Hu (2009), Variability of repeating earthquake behavior along the Longitudinal Valley fault zone of eastern Taiwan, *J. Geophys. Res.*, *114*, B05306, doi:10.1029/2007JB005518.

Chen, Y., K. H. Chen, J. C. Hu and J. C. Lee (2020), Probing the variation in aseismic slip behavior around an active suture zone: observations of repeating earthquakes in Eastern Taiwan, *J. Geophys. Res. Solid Earth*, *125*(5), doi:10.1029/2019JB018561.

Dal Zilio, L., N. Lapusta and J. P. Avouac (2020), Unraveling scaling properties of slow-slip events, *Geophys. Res. Lett.*, *47*, doi:10.1029/2020GL087477.

Dixon, T. H., Y. Jiang, R. Malservisi, R. McCaffrey, N. K. Voss, M. Protti and V. Gonzalez (2014), Earthquake and tsunami forecasts: Relation of slow slip events to subsequent earthquake rupture, *Proc. Natl. Acad. Sci. U.S.A.*, *111*, 17,039–17,044.

Fasola, S. L., M. R. Brudzinski, S. G. Holtkamp, S. E. Graham and E. Cabral-Cano (2019), Earthquake swarms and slow slip on a sliver fault in the Mexican subduction zone, *Proc. Natl. Acad. Sci. U.S.A.*, *116*(15), 7198–7206.

Frank, W. B. and E. E. Brodsky (2019), Daily measurement of slow slip from low-frequency earthquakes is consistent with ordinary earthquake scaling, *Sciences Advances*, *5*(10), eaaw9386.

Freed, A. M. and J. Lin (2001), Delayed triggering of the 1999 Hector Mine earthquake by viscoelastic stress transfer, *Nature*, *411*, 180–183.

Gao, H., D. A. Schmidt and R. J. Weldon (2012), Scaling relationships of source parameters for slow slip events, *Bull. Seismol. Soc. Am.*, *102*(1), 352–360.

Gualandi, A., C. Nichele, E. Serpelloni, L. Chiaraluce, D. Latorre, M. E. Belardinelli and J. P. Avouac (2017), Aseismic deformation associated with an earthquake swarm in the northern Apennines (Italy), *Geophys. Res. Lett.*, *42*, doi:10.1002/2017GL073687.

Hawthorne, J. C. and A. M. Rubin (2010), Tidal modulation of slow slip in Cascadia, *J. Geophys. Res.*, *115*, B09406, doi:10.1029/2010JB007502.

Hayes, G. P., K. P. Furlong, H. M. Benz and M. W. Herman (2014), Triggered aseismic slip adjacent to the 6 February 2013 M_w 8.0 Santa Cruz Islands megathrust earthquake, *Earth Planet. Sci. Lett.*, *388*, 265–272.

Herring, T., W. King and S. M. McCluskey (2010), Introduction to GAMIT/GLOBK release 10.4., *Mass. Inst. of Technol., Cambridge.*

Hsu, Y. J., Y. S. Chang, C. C. Liu, H. M. Lee, A. T. Linde, S. Sacks, G. Kitagawa and Y. G. Chen (2015), Revisiting borehole strain, typhoons, and slow earthquakes using quantitative estimates of precipitation-induced strain changes, *J. Geophys. Res. Solid Earth*, *120*(6), 4556–4571.

Institute of Earth Sciences, Academia Sinica, Taiwan (1996), Broadband Array in Taiwan for Seismology. Institute of Earth Sciences, Academia Sinica, Taiwan. Other/Seismic Network, doi:10.7914/SN/TW.

King, G. C. P., R. S. Stein and J. Lin (1994), Static stress changes and the triggering of earthquakes, *Bull. Seismol. Soc. Am.*, *84*(3), 935–953.

Lee, J. C., J. Angelier, H. T. Chu, J. C. Hu, F. S Jeng and R. J.Rau (2003), Active fault creep variations at Chihshang, Taiwan, revealed by creep meter monitoring, 1998-2001, *J. Geophys. Res.*, *108*(B11), 2528, doi:10.1029/2003JB002394.

Lengliné, O. and D. Marsan (2009), Inferring the coseismic and postseismic stress changes caused by the 2004 M_w=6 Parkfield earthquake from variations of recurrence times of microearthquakes, *J. Geophys. Res.*, 114, B10303, doi:10.1029/2008JB006118.

Lin, J. and R. S. Stein (2004), Stress triggering in thrust and subduction earthquakes and stress interaction between the southern San Andreas and nearby thrust and strike-slip faults, *J. Geophys. Res.*, B02303, doi:10.1029/2003JB002607.

Lin, J. T., K. S. Aslam, A. M. Thomas and D. Melgar (2020), Overlapping regions of coseismic and transient slow slip on the Hawaiian décollement, *Earth Planet. Sci. Lett.*, *544*, doi:10.1016/j.epsl.2020.116353.

Linde, A. T., M. T. Gladwin, M. J. S. Johnston, R. L. Gwyther and R. G. Bilham (1996), A slow earthquake sequence on the San Andreas fault, *Nature*, *383*, 65–68.

Liu, C. C., A. T. Linde and I. S. Sacks (2009), Slow earthquakes triggered by typhoons, *Nature*, *459*, 833–836.

Madariaga, R. (1977), Implications of stress-drop models of earthquakes for the inversion of stress drop from seismic observations, *Pure and Applied Geophysics*, *115*, 301–316.

Michel, S., A. Gualandi and J. P. Avouac (2019), Similar scaling laws for earthquakes and Cascadia slow-slip events, *Nature*, *574*, doi:10.1038/s41586-019-1673-6.

Mouyen, M., A. Canitano, B. F. Chao, Y. J. Hsu, P. Steer, L. Longuevergne and J. P. Boy (2017), Typhoon-induced ground deformation, *Geophys. Res. Lett.*, *44*(21), 11,004–11,011.

Murase, M., N. Matta, C. H. Lin, W. S. Chen and N. Koizumi (2013), An episodic creep-slip event detected by precise levelling surveys in the central part of the Longitudinal Valley Fault, eastern Taiwan, in 2011-2012, *Tectonophysics*, *2013*, 904–913.

Okada, Y. (1992), Internal deformation due to shear and tensile faults in a half-space, *Bull. Seism. Soc. Am.*, *82*(2), 1018–1040.

Peng, Z. and J. Gomberg (2010), An integrated perspective of the continuum between earthquakes and slow-slip phenomena, *Nat. Geosc.*, doi:10.1038/NGEO940.

Perfettini, H., J. P. Avouac, H. Tavera, A. Kositsky, J. M. Nocquet, F. Bondoux, M. Chlieh, A. Sladen, L. Audin, D. L. Farber and P. Soler (2010), Seismic and aseismic slip on the Central Peru megathrust, *Nature*, *465*, 78–81.

Peyret, M., S. Dominguez, R. Cattin, J. Champenois, M. Leroy and A. Zajac (2011), Present-day interseismic surface deformation along the Longitudinal Valley, eastern Taiwan, from a PS-InSAR analysis of the ERS satellite archives, *J. Geophys. Res.*, *116*, B03402, doi:10.1029/2010JB007898.

Radiguet, M., H. Perfettini, N. Cotte, A. Gualandi, B. Valette, V. Kostoglodov, T. Lhomme, A. Walspersdorf, E. Cabral Cano and M. Campillo (2016), Triggering of the 2014 M_w 7.3 Papanoa earthquake by a slow slip event in Guerrero, Mexico, *Nat. Geosc.*, doi:10.1038/NGEO2817.

Rolandone, F., J. M. Nocquet, P. A. Mothes, P. Jarrin, M. Vallée, N. Cubas, S. Hernandez, M. Plain, S. Vaca and Y. Font (2018), Areas prone to slow slip events impede earthquake rupture propagation and promote afterslip, *Sci. Adv.*, *4*, eaao6596.

Sacks, S., S. Suyehiro, D. W. Evertson and Y. Yamagishi (1971), Sacks-Evertson strainmeter, its installation in Japan and some preliminary results concerning strain steps, *Pap. Meteorol. Geophys.*, *22*, 195–208.

Segou, M. and T. Parsons (2018), Testing earthquake links in Mexico from 1978 to the 2017 $M = 8.1$ Chiapas and $M = 7.1$ Puebla shocks, *Geophys. Res. Lett.*, *45*, 708–714.

Segou, M. and T. Parsons (2020), The role of seismic and slow slip events in triggering the 2018 M7.1 Anchorage earthquake in the Southcentral Alaska subduction zone, *Geophys. Res. Lett.*, doi:10.1029/2019GL086640.

Thomas, M. Y., J. P. Avouac, J. Champenois, J. C. Lee and L. C. Kuo (2014), Spatiotemporal evolution of seismic and aseismic slip on the Longitudinal Valley Fault, Taiwan, *J. Geophys. Res.*, *119*(6), 5114–5139.

Thomas, M. Y., J. P. Avouac and N. Lapusta (2017), Rate-and-state friction properties of the Longitudinal Valley Fault from kinematic and dynamic modeling of seismic and aseismic slip, *J. Geophys. Res.*, *122*, doi:10.1002/2016JB013615.

Toda, S, R. S. Stein, K. Richards-Dinger and S. Bozkurt (2005), Forecasting the evolution of seismicity in southern California: Animations built on earthquake stress transfer, *J. Geophys. Res.*, *110*, B05S16, doi:10.1029/2004JB003415.

Uchida, N. and R. Bürgmann (2019), Repeating earthquakes, *Annu. Rev. Earth Planet Sci.*, *47*, doi:10.1146/annurev-earth-053018-060119.

Vallée, M., J. M. Nocquet, J. Battaglia, Y. Font, M. Segovia, M. Régnier, P. Mothes, P. Jarrin, D. Cisneros, S. Vaca, H. Yepes, X. Martin, N. Béthoux and M. Chlieh (2013), Intense interface seismicity triggered by a shallow slow slip event in the Central Ecuador subduction zone, *J. Geophys. Res.*, *118*, 2965–2981.

Voss, N. K., R. Malservisi, T. H. Dixon and M. Protti (2017), Slow slip events in the early part of the earthquake cycle, *J. Geophys. Res. Solid Earth*, *122*(8), 6773–6786.

Waldhauser, F. and W. L. Ellsworth (2000), A double-difference earthquake location algorithm: method and application to the northern Hayward fault, *Bull. Seism. Soc. Am.*, *90*(6), 1353–1368.

Wessel, P. and W. H. F. Smith (1998), New, improved version of the Generic Mapping Tools released, *Eos Trans. AGU*, *79*, 579, doi:10.1029/98EO00426.

Yang, H., L. Zhu and R. Chu (2009), Fault-plane determination of the 18 April 2008 Mount Carmel, Illinois, earthquake by detecting and relocating aftershocks, *Bull. Seism. Soc. Am.*, *99*(6), 3413–3420.

Yarai, H. and S. Ozawa (2013), Quasi-periodic slow slip events in the afterslip area of the 1996 Hyuga-nada earthquakes, Japan, *J. Geophys. Res.*, *118*, 2512–2527.

Yu, S. B., H. Y. Chen and L. C. Kuo (1997), Velocity field of GPS stations in the Taiwan area, *Tectonophysics*, *274*, 51–59.

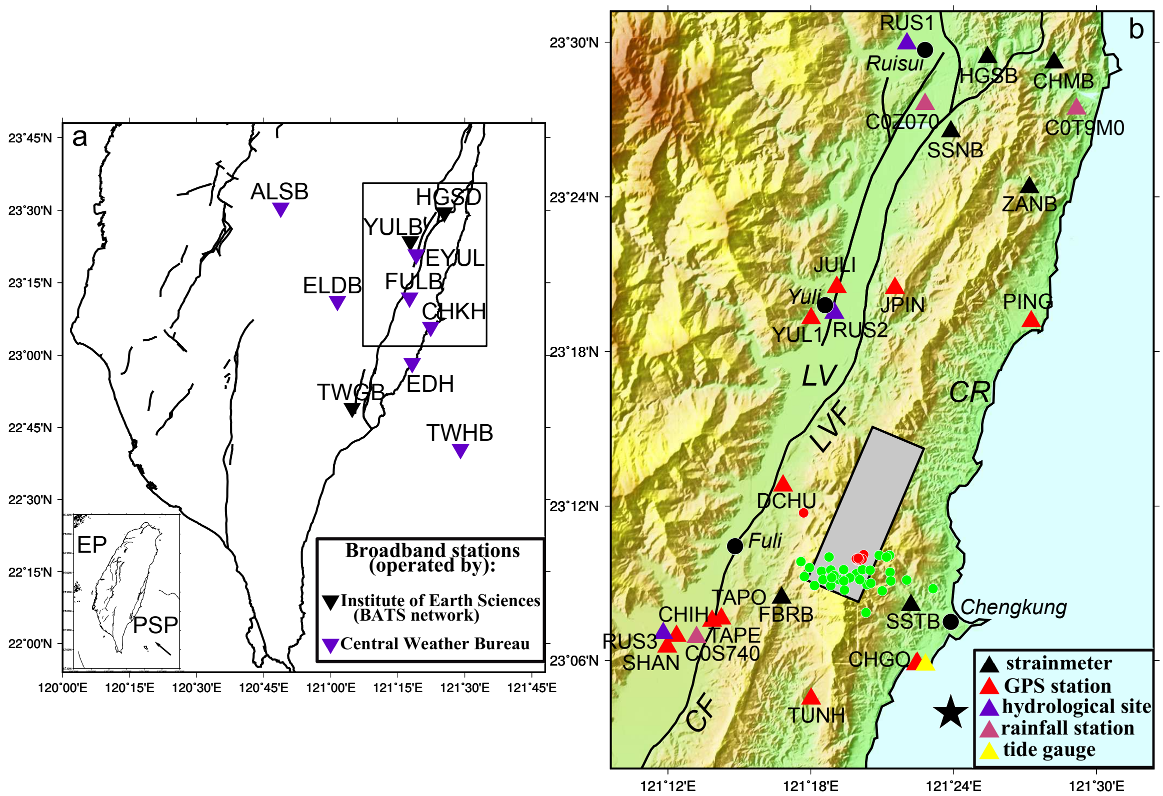

Figure 1. (a) Map of southern Taiwan. Inverted triangles denote broadband seismometers used in this study. (Inset) Geodynamic framework of Taiwan. Black arrow indicates relative motion between Philippine Sea plate (PSP) and Eurasian plate (EP). Black box shows the area in (b). (b) Map of the Longitudinal Valley. Gray rectangle indicates the surface projection of the SSE fault plane. Green and red dots represent the earthquake multiplet before and after relocation, respectively (Section 5). Black star denotes the epicenter location of the Chengkung earthquake. LV: Longitudinal Valley; CR: Coastal Range; LVF: Longitudinal Valley fault; CF: Chihshang fault.

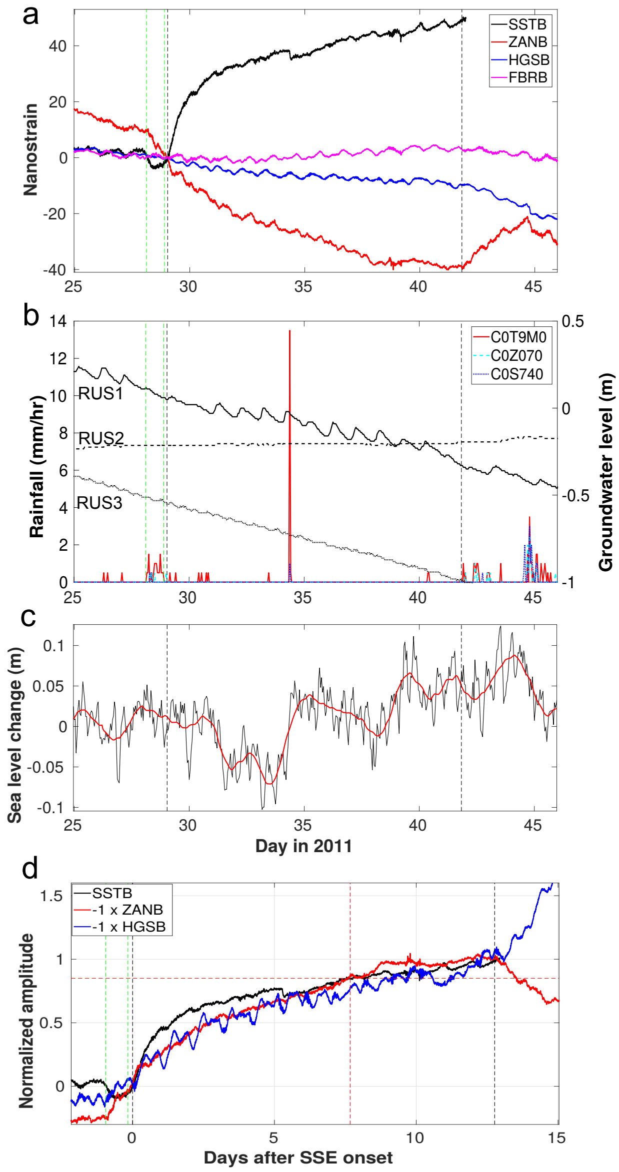

Figure 2. Signals recorded from 01/25 to 02/15/2011: (a) Residual dilatation signals (expansion strain > 0), (b) hourly rainfall and groundwater level variations (black curves), and (c) detided sea level variations (black curve) and smoothed signal (red curve). Vertical black and green dashed lines indicate the SSE episode duration (around days 29.06 to 41.8) and the light rainfall period, respectively. (d) Dilatation signals from 01/27 to 02/13/2011 normalized by the value reached at the end of the SSE episode (ZANB and HGSB are inverted). Vertical red dashed lines indicates the timing of repeaters, occurring when 85% of aseismic slip (6.35 cm) was relieved (horizontal red dashed line).

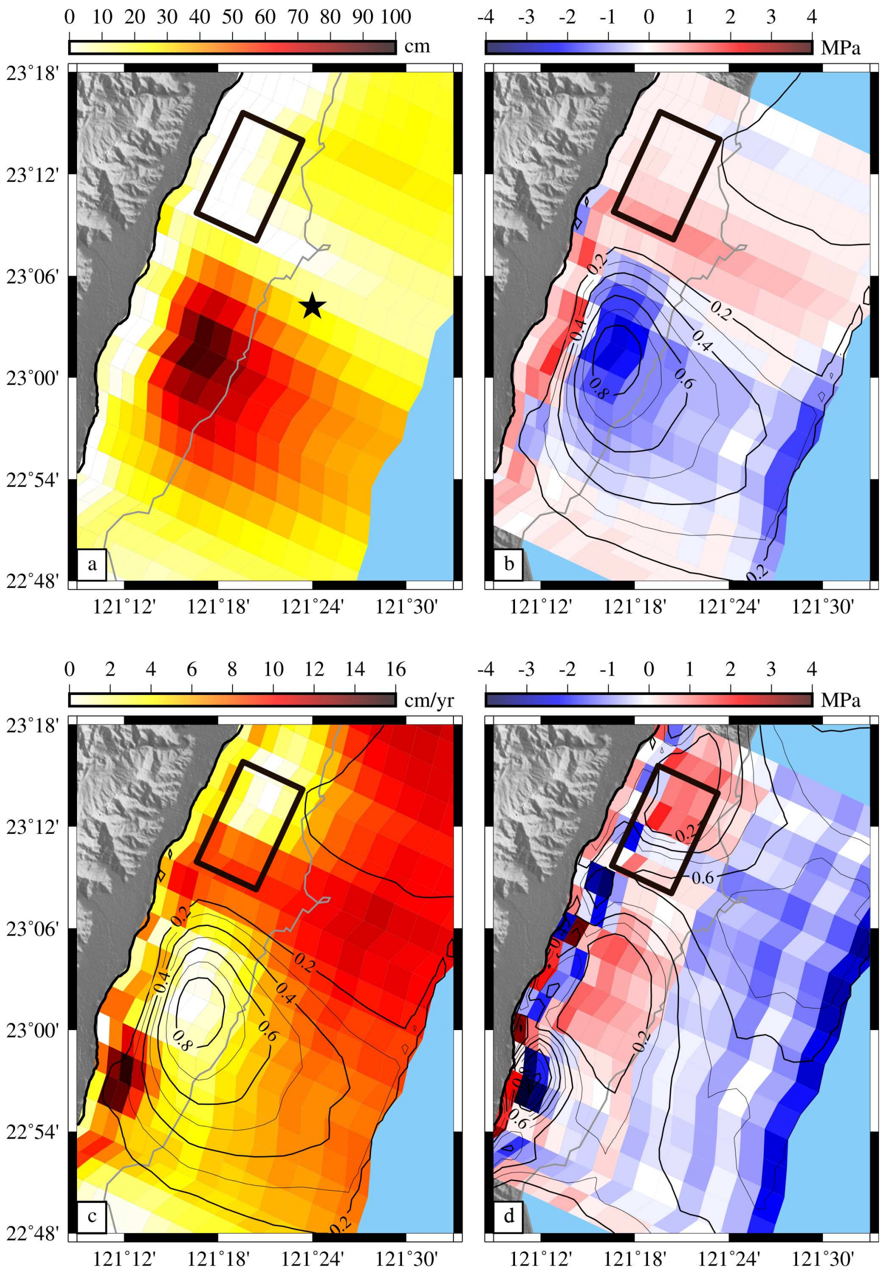

Figure 3. (a) Coseismic and (c) 7-year postseismic (12/2003-11/2010) slip models of the 2003 Chengkung earthquake. Static Coulomb stress changes imparted by (b) coseismic and (d) postseismic slip resolved onto the LVF fault plane. Black rectangle outlines the SSE rupture area and black star denotes the epicenter location of the Chengkung earthquake. Black curves show the contour lines of coseismic slip distribution (in meter) in (b) and (c) and final postseismic slip distribution (in meter) in (d).

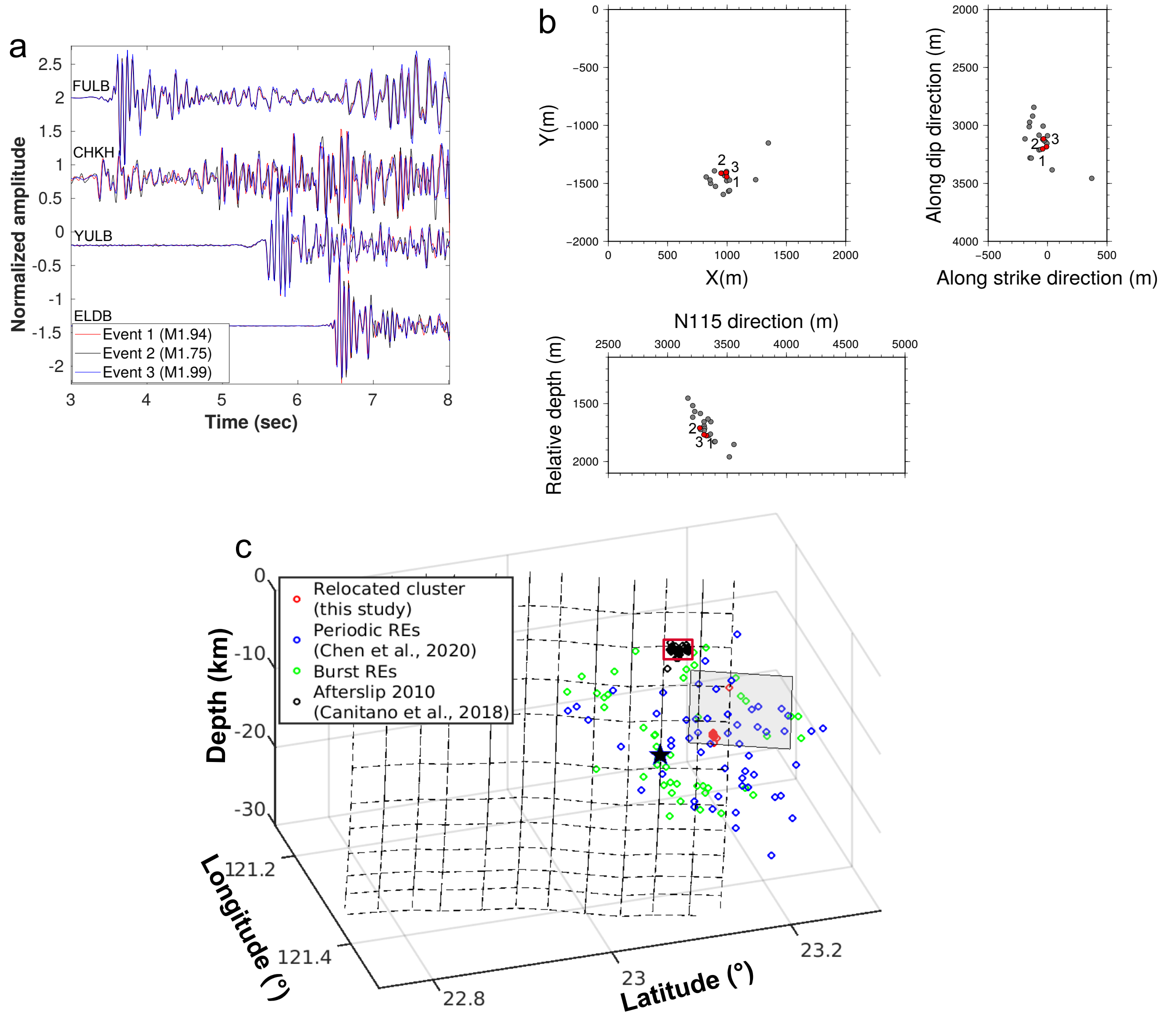

Figure 4. (a) Multiplets identified during the SSE episode. (b) Double-difference relocation of the earthquake cluster. (Left) Longitude-latitude map of the seismicity. (Right) Projection of the seismicity on the LVF fault plane. (Bottom) Cross-section perpendicular to the LVF. Red and grey dots denote events identified during the SSE episode and the other events of the cluster, respectively. (c) Aseismic and seismic activities possibly affected by the 2003 Chengkung earthquake (black star). Periodic REs and REs bursts are events with $M_L \geq 2$ for the 2000-2011 period (see *Chen et al.* [2020] for details). Gray and plain red rectangles outline the 2011 SSE and 2010 afterslip fault planes, respectively.